



A noise-optimized virtual monoenergetic reconstruction algorithm improves the diagnostic accuracy of late hepatic arterial phase dual-energy CT for the detection of hypervascular liver lesions

Carlo N. De Cecco¹ · Damiano Caruso^{1,2} · U. Joseph Schoepf¹  · Domenico De Santis^{1,2} · Giuseppe Muscogiuri^{1,3} · Moritz H. Albrecht^{1,4} · Felix G. Meinel^{1,5} · Julian L. Wichmann^{1,4} · Philip F. Burchett¹ · Akos Varga-Szemes¹ · Douglas H. Sheafor¹ · Andrew D. Hardie¹

Received: 13 July 2017 / Revised: 5 December 2017 / Accepted: 3 January 2018 / Published online: 19 February 2018
© European Society of Radiology 2018

Abstract

Objectives To assess the image quality and diagnostic accuracy of a noise-optimized virtual monoenergetic imaging (VMI+) algorithm compared with standard virtual monoenergetic imaging (VMI) and linearly-blended (M_{0.6}) reconstructions for the detection of hypervascular liver lesions in dual-energy CT (DECT).

Methods Thirty patients who underwent clinical liver MRI were prospectively enrolled. Within 60 days of MRI, arterial phase DECT images were acquired on a third-generation dual-source CT and reconstructed with M_{0.6}, VMI and VMI+ algorithms from 40 to 100 keV in 5-keV intervals. Liver parenchyma and lesion contrast-to-noise-ratios (CNR) were calculated. Two radiologists assessed image quality. Lesion sensitivity, specificity and area under the receiver operating characteristic curves (AUCs) were calculated for the three algorithms with MRI as the reference standard.

Results VMI+ datasets from 40 to 60 keV provided the highest liver parenchyma and lesion CNR ($p \leq 0.021$); 50 keV VMI+ provided the highest subjective image quality (4.40 ± 0.54), significantly higher compared to VMI and M_{0.6} (all $p < 0.001$), and the best diagnostic accuracy in < 1-cm diameter lesions (AUC=0.833 vs. 0.777 and 0.749, respectively; $p \leq 0.003$).

Conclusions 50-keV VMI+ provides superior image quality and diagnostic accuracy for the detection of hypervascular liver lesions with a diameter < 1 cm compared to VMI or M_{0.6} reconstructions.

Key Points

- Low-keV VMI+ are characterized by higher contrast resulting from maximum iodine attenuation.
- VMI+ provides superior image quality compared with VMI or M_{0.6}.
- 50-keV VMI+ provides higher accuracy for the detection of hypervascular liver lesions < 1 cm.

Keywords Dual-energy CT · Hypervascular liver lesions · Virtual monoenergetic images · Diagnostic accuracy · Liver imaging

Abbreviations

CNR	Contrast-to-noise ratio	keV	Kiloelectron volt
DECT	Dual-energy computed tomography	M _{0.6}	Linearly-blended dual energy images
		MRI	Magnetic resonance imaging

Electronic supplementary material The online version of this article (<https://doi.org/10.1007/s00330-018-5313-6>) contains supplementary material, which is available to authorized users.

✉ U. Joseph Schoepf
schoepf@muscc.edu

¹ Department of Radiology and Radiological Science, Medical University of South Carolina, 25 Courtenay Drive, Charleston, SC, USA

² Department of Radiological Sciences, Oncological and Pathological Sciences University of Rome “Sapienza”, Latina, Italy

³ Department of Clinical and Molecular Medicine, University of Rome “Sapienza”, Rome, Italy

⁴ Department of Diagnostic and Interventional Radiology, University Hospital Frankfurt, Frankfurt am Main, Germany

⁵ Institute for Clinical Radiology, Ludwig Maximilian University Hospital, Munich, Germany

VMI Virtual monoenergetic images
 VMI+ Noise-optimized virtual monoenergetic images

Introduction

Dual-energy computed tomography (DECT) has the potential to generate virtual monoenergetic images at specific kiloelectron volt (keV) levels ranging from 40 keV to 190 keV, reconstructed from the combination of two acquisitions with different tube potentials [1, 2]. Low keV level virtual monoenergetic images are characterized by higher contrast resulting from maximum iodine attenuation (close to the K edge of iodine at 33.2 keV), leading to improved liver lesions conspicuity [3–5]. Sudarski et al. [6] and Yamada et al. [7] have previously described the usefulness of standard virtual monoenergetic images (VMI), reporting that peak contrast-to-noise ratios (CNRs) for liver parenchyma and focal liver lesions occurred at 70 keV, resulting from the higher attenuation and lower image noise. Nevertheless, VMI datasets below 70 keV have been reported to be adversely affected by high image noise, limiting clinical application [8, 9].

Recently, an advanced noise-optimized virtual monoenergetic reconstruction algorithm (VMI+) has been developed to overcome this technical limitation [10]. The VMI+ algorithm combines the greater iodine attenuation of the standard VMI algorithm at low virtual photon energies with the lower image noise at higher virtual photon energies, ultimately resulting in a higher CNR at low virtual photon energies. Marin et al. confirmed the higher CNR at 40 keV for hypervascular liver lesions by using the VMI+ algorithm compared to standard VMI reconstruction [11]. However, whether these differences in image quality translate into an improved detection rate of hypervascular liver lesions remains unknown.

Thus, this study sought to assess the image quality and diagnostic accuracy of a noise-optimized VMI+ algorithm in comparison with standard VMI and linearly-blended reconstructions for the detection of hypervascular liver lesions in late hepatic arterial-phase DECT.

Materials and methods

Patient population

This prospective, single-centre study was approved by our local Institutional Review Board and conducted in compliance with the Health Insurance Portability and Accountability Act. All patients provided written informed consent before enrolment.

Between September 2014 and February 2015, consecutive patients with known or suspected hypervascular liver lesions

who underwent a clinically indicated magnetic resonance imaging (MRI) examination of the liver were enrolled in the study. MRI was considered the reference standard. Additional details on the reference standard rationale and MRI technique are available in the [Online Appendix](#). Inclusion and exclusion criteria are listed in Supplemental Table 1.

Radiation dose

The dose length product (DLP) of the late arterial phase, automatically provided in the scan protocol, was recorded for each examination. Effective radiation dose (ED) was calculated by multiplying the DLP with an abdomen-specific conversion coefficient k of $0.015 \text{ mSv} \cdot \text{mGy}^{-1} \cdot \text{cm}^{-1}$ [12].

CT technique

A third-generation dual-source CT scanner was used for all CT studies (Somatom Force; Siemens Healthineers, Forchheim, Germany) in dual-energy (DE) mode. The acquisitions were conducted in a cranio-caudal direction from the diaphragmatic dome to the iliac crests. The following parameters were used for the DE arterial phase: tube settings 100/150Sn kVp and 180/90 mAs, respectively, equipped with an integrated tin filter (Selective Photon Shield II, SPS II, Siemens); pitch 0.7; collimation $2 \times 64 \times 0.6 \text{ mm}$ for both detectors; field-of-view 350 mm. Automated real-time anatomical tube current modulation (CARE Dose 4D, Siemens) was selected in all acquisitions.

Contrast media (Omnipaque 350 mgI/ml, GE Healthcare, Milwaukee, WI, USA) was injected at a flow rate of 4 ml/s, followed by a 30-ml saline chaser using a dual-syringe power injector (Stellant D CT Injection System, Medrad, Inc., Warrendale, PA, USA) through an 18-gauge access placed in a superficial vein in the antecubital fossa, adapting the amount of contrast media to the BMI [13]. For subjects with a body mass index (BMI) less than 30 kg/m^2 , a contrast volume of 100 ml was administered, whereas 120 ml was administered for subjects with a BMI greater than 30 kg/m^2 . A dedicated bolus-tracking technique application (CARE Bolus, Siemens) was used to set the timing of acquisition with a region-of-interest (ROI) drawn in the abdominal aorta at the level of the diaphragmatic dome. A threshold of 100 Hounsfield units (HU) for the tracking scan (100 kVp, 23 mAs) was used with an 18-s delay for the late arterial phase and 70-s delay for the portal venous phase. Only the DE late arterial phase datasets were analysed in this research study.

Image reconstruction

All raw data were transferred to a three-dimensional workstation (*syngo.via*, version VA30, Siemens). DECT datasets were

reconstructed using an abdominal soft tissue convolution kernel (Qr40) with a section thickness of 3.0 mm and an increment of 2.0 mm. Three image series were reconstructed for the purpose of the study. The first image series was designed to simulate the traditional clinical routine single-energy 120 kVp by using vendor-recommended settings to create linearly-blended images (M_0.6), combining 60% of low tube voltage and 40 % of high tube voltage data. The second and the third image series were reconstructed as a standard VMI and noise-optimized VMI+ dataset, respectively, using a clinically available DE application (*syngo.via* Dual Energy workflow, version VA30, Siemens), at energy levels ranging from 40 keV to 100 keV with 5-keV increments. Higher keV levels were not investigated mainly due to the lower attenuation previously reported [4, 10]. For each dataset, iterative reconstruction (ADMIRE, Siemens Healthcare) was used with a strength level of 3.

Objective image analysis

All measurements were performed on a multi-modality workstation (*syngo.via*, version VA30, Siemens). Liver attenuation values in HU were recorded by one radiologist with 7 years of experience in abdominal imaging, by drawing three 1-cm² circular ROIs in the liver parenchyma (segments II, VII and VIII) avoiding great vessels and lesions. Additionally, two 1-cm² circular ROIs were drawn within the paired para-spinal musculature at the level of L2. The liver parenchyma and paravertebral muscle ROIs were separately averaged. Image noise was recorded as the standard deviation in the left-sided pararenal fat. The DE application enabled automatic recording of all attenuation numbers and image noise values within a single ROI for all keV levels, consequently reducing the variance in multiple measurements. Liver CNR was obtained using the following formula [14]:

$$\text{Liver CNR} = \frac{(HU_{\text{liver}} - HU_{\text{muscle}})}{SD_{\text{fat}}}$$

The same radiologist (not blinded to the patient records) analysed all hypervascular lesions reported by drawing an as large as possible circular ROI without exceeding the lesion size. CNR of hypervascular lesions was obtained as previously described [15]:

$$\text{Lesion CNR} = \frac{(HU_{\text{lesion}} - HU_{\text{liver}})}{SD_{\text{fat}}}$$

Subjective image analysis

Based on the objective image quality results, subjective image quality was assessed for M_0.6, VMI at 70 and 75 keV, and VMI+ at 40–60 keV every 5 keV, since we observed the

highest CNR values without statistical differences among these image series. To avoid recall bias, image series were randomized and evaluated at least 2 weeks between reading sessions. Two other independent readers with 10 and 8 years of experience in abdominal imaging, blinded to MRI results, patient records and image reconstructions, performed image quality assessment and lesion detection analysis. Image evaluation was performed individually in separate reading sessions. Window settings were manually adjustable by the radiologist if needed. Image quality was assessed, according to reader perception, with a 5-point Likert scale [16] based on the following score system: 1= insufficient for diagnosis; 2= substandard; low diagnostic confidence; 3= acceptable; 4= above average, good diagnostic confidence; 5= excellent. Overall diagnostic image quality was represented as the sum of the single variables score (sharpness, image noise and lesion conspicuity; Supplemental Table 2). An inter-reader agreement analysis was also performed.

Diagnostic accuracy

After a 3-month interval, the two readers who had previously performed the subjective image assessment were asked to independently evaluate the presence of hypervascular liver lesions stratified by size (< 1 cm and ≥ 1 cm). For the evaluation of diagnostic accuracy, the keV reconstructions with the highest objective and subjective image quality for each dataset were selected. Readers were blinded to patient records and image reconstructions. Lesion-based sensitivity and specificity were calculated for both readers and averaged between them. Eventually, areas under the receiver operating characteristic (ROC) curves (AUCs) of the three datasets were calculated.

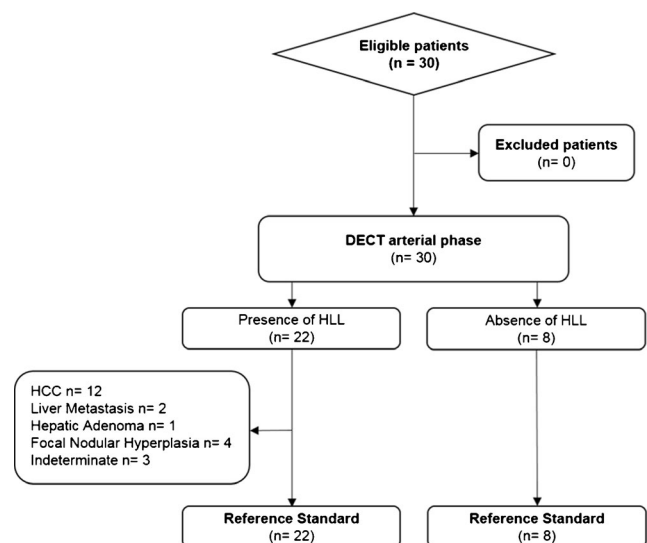


Fig. 1 Flow diagram of patient recruitment. MRI was used as reference standard. DECT dual-energy computed tomography, HCC hepatocellular carcinoma, HLL hypervascular liver lesions

Table 1 Patient characteristics

Parameter	Patients (n= 30)
Demographic	
Age, mean (range), y	58.8 ± 10.2 (37–74)
Male-to-female ratio	17:13
Body weight, mean (range), kg	82.4 ± 18.8 (52–125)
Body mass index, mean (range), kg/m ²	28.2 ± 4.9 (19–38)
MRI-based diagnosis (number of patients)	
Hepatocellular carcinoma	12
Hypervascular liver metastasis	2
Hepatic adenoma	1
Focal nodular hyperplasia	4
Indeterminate	3

An inter-reader agreement analysis was performed to assess reproducibility of the technique.

Statistical analysis

Statistical analysis was performed using MedCalc Statistical Software version 16.8.4 (MedCalc Software bvba, Ostend, Belgium). Continuous variables are displayed as mean ±

standard deviation; categorical variables are conveyed as frequencies and percentages. A Kolmogorov-Smirnov test was used to assess data distribution.

Per-lesion sensitivity and specificity of VMI+, VMI and M_{0.6} datasets were calculated with 95 % confidence intervals and compared using McNemar's test. The capability of the datasets for the identification of hypervascular liver lesions was evaluated on a per-lesion basis using the AUCs with MRI being the reference standard. Comparison among the AUCs was performed using DeLong's method [17]. A repeated-measures analysis of variance test (ANOVA) was used to assess differences in objective image quality, tested between M_{0.6} images and VMI and VMI+ reconstructions and evaluated at each keV level. A post-hoc Bonferroni test was performed when significant differences were observed. Subjective image quality was analysed by averaging the two readers' 5-point scores and using the nonparametric Friedman test with post-hoc tests. Inter-reader agreement on subjective image quality scores and number of detected lesions was evaluated using the Cohen kappa (κ) statistics explained as follow: ≤ 0.20 , slight agreement; 0.21–0.40, fair agreement; 0.41–0.60, moderate agreement; 0.61–0.80, good agreement; ≥ 0.81 , excellent agreement. Two-tailed p -values < 0.05 were considered statistically significant.

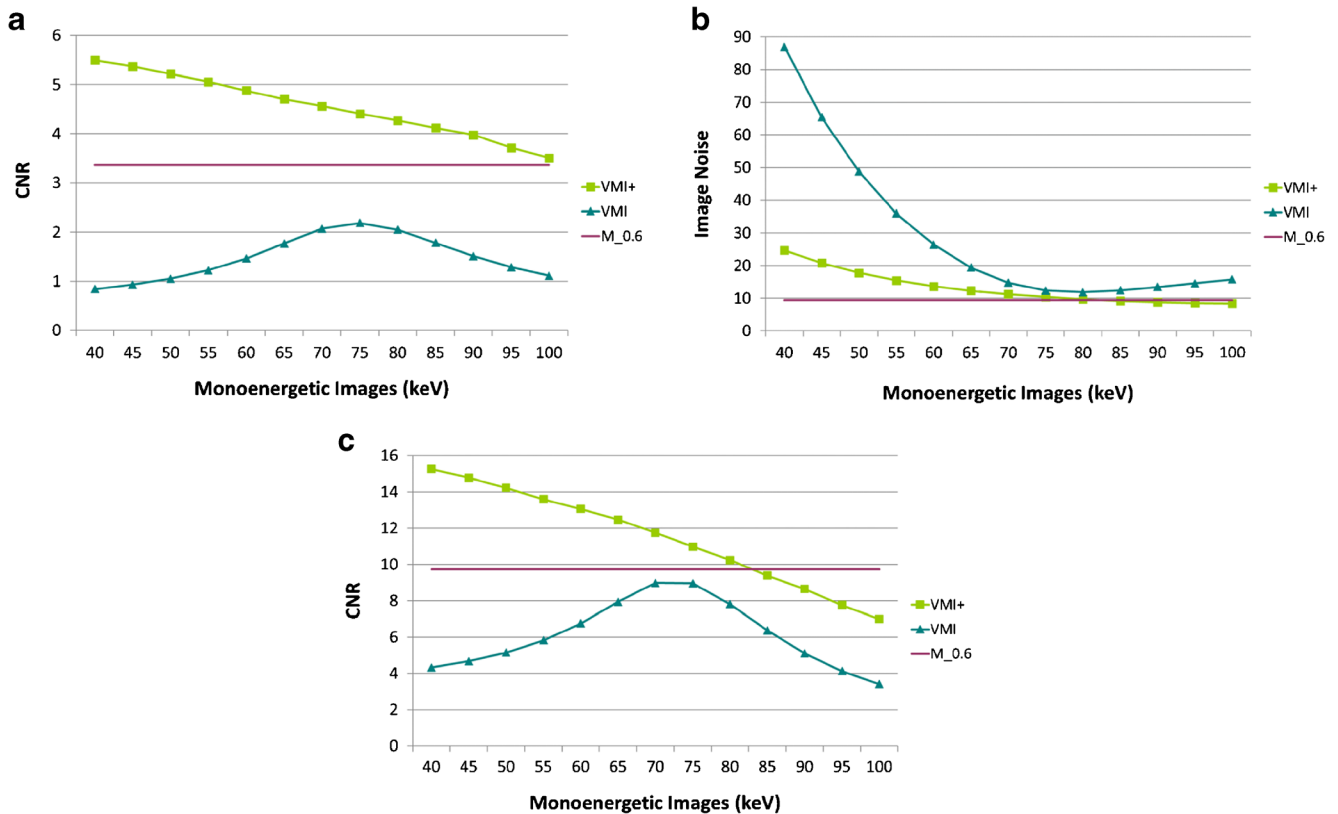


Fig. 2 (a) Liver parenchyma CNR, (b) image noise and (c) hypervascular liver lesion contrast-to-noise ratios (CNRs) at different keV levels. Plots compare standard (VMI) and noise-optimized (VMI+) monoenergetic images. The horizontal line represents the linearly-blended images (M_{0.6})

0.6). VMI+ images are characterized by an overall lower image noise than VMI, moreover VMI+ dataset at low keV provided substantially higher liver- and lesion-to-liver CNR than VMI at 70 keV

Results

Patient population

A total of 30 patients (17 males and 13 females, mean age 58.8 years) were prospectively enrolled in this study. The average time between the MRI and DECT examination was 17 days (range 1–50 days). The average number of lesions per patient was 3.6 (range 1–8). No patient experienced early adverse reaction to the administration of MRI or CT contrast media. Figure 1 and Table 1 show further patient details.

Radiation dose

The mean DLP was 207.1 ± 90.3 mGy · cm (range 74.3–371.5 mGy · cm), for an estimated mean ED of 3.0 ± 1.4 mSv.

Objective image analysis

The highest CNR for liver parenchyma was observed at 40 keV for VMI+ images (5.50 ± 2.65) (Fig. 2a), showing significant improvement compared to highest parenchymal CNR for VMI at 75 keV ($p=0.021$). No significant differences in liver parenchyma with VMI+ were observed between 40–60 keV (all $p \geq 0.11$), whereas all CNR values were significantly higher compared to the standard M_0.6 (3.36 ± 2.82 ; $p < 0.001$). Instead, VMI images showed significantly inferior liver CNR values compared to the standard M_0.6 ($p \leq 0.021$), reported in Table 2, influenced by image noise. M_0.6 dataset had a significantly lower noise compared with VMI at 75 keV (9.75 vs. 12.38, $p = 0.001$) and VMI+ at 40 keV (24.74, $p = 0.001$), whereas VMI+ at 40 keV resulted in an image noise significantly higher than VMI at 75 keV ($p = 0.007$) (Fig. 2b).

Hypervascular liver lesion CNRs reached a peak at 40 keV VMI+ (15.25 ± 19.95), significantly greater than the highest CNR value for VMI at 70 keV (8.98 ± 8.50 , $p < 0.001$) and M_0.6 (9.72 ± 8.24 , $p < 0.001$) (Fig. 2c). No statistical differences were observed between 70 keV VMI and M_0.6 CNR ($p = 0.18$). As previously observed for liver parenchyma, the CNR of hypervascular liver lesions for VMI+ was significantly higher from 40 to 60 keV compared to the other keV intervals (all $p \leq 0.033$), whereas for VMI no significant differences were found between 70 keV and 75 keV ($p = 0.87$) (Fig. 3). Full results of liver lesion CNRs are listed in Table 2.

Subjective image analysis

Table 3 shows the comparison of the averaged scores for both readers among the different datasets. The determinant values of the subjective image quality are reported in Table 4.

Table 2 CNR values of liver parenchyma and hypervascular liver lesions for noise-optimized (VMI+) and standard (VMI) monoenergetic algorithms as well as for linearly-blended images (M_0.6)

Dataset	40 keV	45 keV	50 keV	55 keV	60 keV	65 keV	70 keV	75 keV	80 keV	85 keV	90 keV	95 keV	100 keV
Liver													
VMI+	5.50 ± 2.65	5.37 ± 2.54†	5.22 ± 2.43†	5.06 ± 2.36†	4.88 ± 2.31†	4.71 ± 2.30	4.56 ± 2.33	4.41 ± 2.36	4.27 ± 2.42	4.12 ± 2.47	3.98 ± 2.53	3.72 ± 2.49	3.51 ± 2.47
VMI	0.84 ± 0.70	0.93 ± 0.76	1.05 ± 0.86	1.23 ± 0.99	1.46 ± 1.19	1.77 ± 1.44	2.07 ± 1.70†	2.19 ± 1.82	2.05 ± 1.78	1.78 ± 1.65	1.51 ± 1.48	1.28 ± 1.33	1.11 ± 1.20
M_0.6	3.36 ± 2.82												
Liver lesions													
VMI+	15.25 ± 19.95	14.77 ± 18.90†	14.22 ± 17.76†	13.60 ± 16.50†	13.06 ± 15.24†	12.47 ± 13.97	11.75 ± 12.86	10.98 ± 11.73	10.24 ± 10.70	9.39 ± 9.61	8.64 ± 8.67	7.76 ± 7.51	6.99 ± 6.66
VMI	4.33 ± 3.51	4.67 ± 3.86	5.16 ± 4.34	5.83 ± 5.04	6.75 ± 6.01	7.93 ± 7.29	8.98 ± 8.50	8.95 ± 8.77†	7.81 ± 8.24	6.38 ± 7.36	5.11 ± 6.40	4.12 ± 5.57	3.41 ± 5.00
M_0.6	9.72 ± 8.24												

Data are reported as mean scores ± standard deviation

Highest values for each dataset are in bold

† indicates the CNR values with no statistical differences compared to the highest one

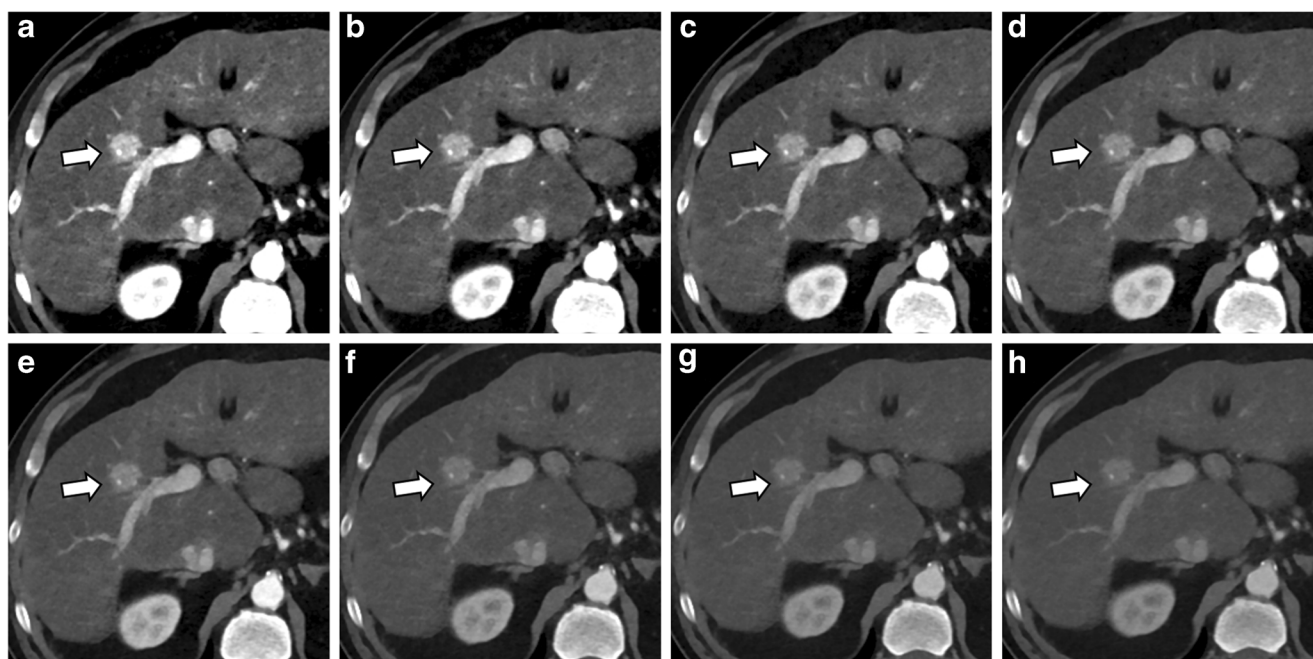


Fig. 3 Dual-energy CT study of the liver in a 63-year-old man with HCC. A hypervascular liver lesion is shown on transverse sections at the most suitable energy levels for VMI+ (a, b, c, d and e; 40 keV, 45 keV, 50 keV, 55 keV and 60 keV, respectively) and VMI (f and g; 70 keV and 75 keV,

respectively), as well as M_{0.6} (h) datasets. Low keV VMI+ images are characterized by higher image contrast in comparison to VMI and M_{0.6} datasets. The window width and level were held constant at 450 and 100, respectively

According to objective image analysis results, subjective image analysis was performed within levels of keV ranging from 40 to 60 for VMI+ and at 70–75 keV for VMI datasets.

The highest overall image quality score averaged between the two readers was significantly greater for 50 keV VMI+ images (4.40 ± 0.54) compared to the highest value of VMI at 70 keV (3.76 ± 0.55 ; $p < 0.001$) and M_{0.6} (3.93 ± 0.44 ; $p < 0.001$). No significant differences were reported between VMI at 70 keV and M_{0.6} ($p > 0.99$).

The inter-reader overall agreement was excellent for VMI+ images at 45, 50 and 55 keV and for VMI images at 70 and 75 keV (all $\kappa > 0.8$), whereas good agreement was reached for

M_{0.6} images ($\kappa = 0.64$). Complete results are reported in Table 4.

Assessment of diagnostic accuracy

Comprehensive details of diagnostic accuracy are available in Table 5. Detailed results for both readers are listed in Supplemental Table 3. A total of 61 hypervascular liver lesions were detected in 30 patients by the reference standard ($n = 36$ for lesions with < 1 cm diameter and $n = 25$ for lesions with ≥ 1 cm) (Fig. 4). All CT examinations were included in the analysis.

Table 3 Full comparison of overall subjective image quality averaged between the two readers and expressed as mean \pm standard deviation (SD)

Subjective image quality	Mean \pm SD	<i>p</i> -value (Friedman test)							
		40 keV VMI+	45 keV VMI+	50 keV VMI+	55 keV VMI+	60 keV VMI+	70 keV VMI	75 keV VMI	M _{0.6}
40 keV VMI+	4.07 ± 0.47		0.001*	0.002*	0.004*	> 0.99	0.006*	0.004*	> 0.99
45 keV VMI+	4.26 ± 0.52	0.001*		0.63	0.89	0.005*	< 0.001*	< 0.001*	0.046*
50 keV VMI+	4.40 ± 0.54	0.002*	0.63		> 0.99	< 0.001*	< 0.001*	< 0.001*	< 0.001*
55 keV VMI+	4.39 ± 0.52	0.004*	0.89	> 0.99		< 0.001*	< 0.001*	< 0.001*	< 0.001*
60 keV VMI+	4.12 ± 0.43	> 0.99	0.005*	< 0.001*	< 0.001*		< 0.001*	< 0.001*	> 0.99
70 keV VMI	3.76 ± 0.55	0.006*	< 0.001*	< 0.001*	< 0.001*	< 0.001*		> 0.99	> 0.99
75 keV VMI	3.75 ± 0.54	0.004*	< 0.001*	< 0.001*	< 0.001*	< 0.001*	> 0.99		0.90
M _{0.6}	3.93 ± 0.44	> 0.99	0.046*	< 0.001*	< 0.001*	> 0.99	> 0.99	0.90	

Asterisks identify significant *p*-values

Table 4 Subjective image quality assessment and inter-reader agreement of both readers

	40 keV VMI+	45 keV VMI+	50 keV VMI+	55 keV VMI+	60 keV VMI+	70 keV VMI	75 keV VMI	M _{0.6}
Reader 1	Mean ± SD							
Overall	4.06 ± 0.55	4.24 ± 0.51	4.39 ± 0.50	4.40 ± 0.50	4.15 ± 0.53	3.75 ± 0.58	3.76 ± 0.59	3.99 ± 0.58
Sharpness	3.86 ± 0.69	4.17 ± 0.66	4.52 ± 0.57	4.48 ± 0.57	4.17 ± 0.76	4.00 ± 0.60	4.03 ± 0.63	4.10 ± 0.56
Noise	4.10 ± 0.62	4.31 ± 0.66	4.45 ± 0.57	4.48 ± 0.57	4.28 ± 0.70	3.86 ± 0.58	3.83 ± 0.54	4.00 ± 0.65
Lesion Conspicuity	4.23 ± 0.82	4.23 ± 0.71	4.15 ± 0.78	4.19 ± 0.80	3.96 ± 0.66	3.31 ± 0.93	3.35 ± 0.98	3.81 ± 0.94
Reader 2	Mean ± SD							
Overall	4.08 ± 0.47	4.28 ± 0.52	4.41 ± 0.54	4.39 ± 0.52	4.09 ± 0.43	3.78 ± 0.55	3.75 ± 0.54	3.87 ± 0.44
Sharpness	4.07 ± 0.70	4.24 ± 0.69	4.55 ± 0.57	4.52 ± 0.57	4.14 ± 0.69	4.00 ± 0.53	3.97 ± 0.57	4.03 ± 0.42
Noise	4.14 ± 0.64	4.31 ± 0.66	4.45 ± 0.63	4.41 ± 0.63	4.17 ± 0.60	3.90 ± 0.56	3.86 ± 0.52	3.86 ± 0.58
Lesion Conspicuity	4.04 ± 0.60	4.23 ± 0.71	4.15 ± 0.78	4.19 ± 0.75	3.96 ± 0.66	3.38 ± 0.90	3.35 ± 0.89	3.65 ± 0.69
Inter-reader agreement (κ)								
Overall	0.58	0.92	0.90	0.85	0.77	0.90	0.82	0.64
Sharpness	0.44	0.90	0.93	0.81	0.86	0.86	0.76	0.35
Noise	0.50	0.96	0.88	0.88	0.74	0.93	0.78	0.55
Lesion Conspicuity	0.74	0.96	0.96	0.93	0.92	0.94	0.94	0.81

Qualitative data are reported as mean ± standard deviation (SD)

Table 5 Comprehensive diagnostic accuracy for the identification of hypervascular liver lesion of VMI+, VMI, and M_0.6 datasets

	VMI+			VMI			M_0.6		
	< 1 cm	≥ 1 cm	All	< 1 cm	≥ 1 cm	All	< 1 cm	≥ 1 cm	All
Se (95 % CI)	69 % (57–80)	92 % (81–98)	79 % (70–86)	58 % (46–70)	90 % (78–97)	71 % (62–79)	53 % (41–65)	88 % (76–95)	67 % (58–75 %)
Sp (95 % CI)	97 % (85–100)	94 % (79–99)	95 % (87–99)	97 % (85–100)	94 % (79–99)	95 % (87–99)	97 % (85–100)	97 % (84–100)	97 % (89–100 %)
AUC (95 % CI)	0.833 (0.748–0.898)	0.929 (0.850–0.974)	0.871 (0.814–0.915)	0.777 (0.686–0.852)	0.919 (0.837–0.968)	0.834 (0.773–0.884)	0.749 (0.656–0.828)	0.924 (0.844–0.971)	0.821 (0.758–0.873)

Se sensitivity, Sp specificity, AUC area under the curve, CI confidence interval

All lesions

The VMI+ dataset provided the highest sensitivity (79 %) in comparison to the VMI (71 %, $p=0.004$) and the M_0.6 algorithm (67 %, $p < 0.001$) for the detection of all hypervascular liver lesions in comparison with MRI as the reference standard. Both the VMI and M_0.6 dataset reported comparable sensitivity ($p = 0.125$). The specificity was similar across the three datasets (95 % for VMI+ and VMI, 97 % for M_0.6; all $p = 1$). The VMI+ dataset obtained the largest AUC (0.871), significantly larger than VMI and M_0.6 (0.834 and 0.821, respectively, all $p = 0.002$) while no difference was found between VMI and M_0.6 ($p = 0.325$) (Fig. 5a).

Overall inter-reader agreement between the two readers was excellent for all image datasets ($\kappa = 0.89, 0.86$ and 0.83 for VMI+, VMI and M_0.6, respectively) (Supplemental Table 3).

Lesions ≥ 1 cm diameter

For lesions with a diameter ≥ 1 cm, the VMI+ dataset provided no significant increment in sensitivity and specificity (92 % and 94 %) in comparison to VMI and M_0.6 datasets (90–94 % and 88–97 %, respectively, all $p \geq 0.5$). The AUCs showed no significant differences among the three protocols (all $p \geq 0.317$) (Fig. 5b).

Lesions < 1 cm diameter

For lesions with a diameter < 1 cm, the VMI+ dataset demonstrated the highest sensitivity (69 %) in comparison to VMI and M_0.6 datasets (58 % and 53 %, respectively, all $p \leq 0.008$). The sensitivity of VMI and M_0.6 datasets was not statistically different ($p = 0.219$). All datasets accounted for the same specificity (97 %, $p = 1$). The VMI+ dataset showed a significantly larger AUC (0.833) compared to the VMI and M_0.6 datasets (0.777 and 0.749, respectively; $p = 0.003$ and $p < 0.001$, respectively). No significant differences were found between the AUCs of VMI and M_0.6 ($p = 0.098$) (Fig. 5c).

Discussion

The aim of our study was to assess the image quality and diagnostic accuracy of DECT images reconstructed with VMI+, VMI, and linearly-blended M_0.6 algorithms for the detection of hypervascular liver lesions, utilizing MRI as the reference standard. Our findings demonstrate that the 50 keV VMI+ dataset provides both greater objective and subjective image quality and also an improved diagnostic accuracy for lesions with a diameter < 1 cm, compared to VMI and M_0.6 datasets. Thus, the results of this prospective study indicate

that 50-keV VMI+ images may be beneficial in the detection of hypervascular liver lesions and should be preferred over the other DECT reconstruction techniques and settings.

On a lesion-based analysis, 50 keV VMI+ demonstrated a 64 % higher lesion CNR compared to the standard 70 keV VMI and a 52 % higher CNR in comparison with M_0.6 images. The VMI+ algorithm provided higher lesion CNR in comparison to VMI images at every other energy level assessed, showing comparable values in an intra-dataset analysis for energy levels ranging from 40–60 keV, while VMI datasets provided the highest CNR at 70 keV and 75 keV. It should be noted that there was no significant difference between VMI and M_0.6 series regarding liver lesion CNRs despite the higher liver lesion attenuation observed for VMI, because of the significant increment in image noise of the VMI dataset. Despite a CNR peak at 40 keV, both readers preferred the 50 keV VMI+ images in subjective image quality analysis, with significant differences when compared to other VMI+ energy levels, 70 keV VMI and M_0.6 images. Different investigators have demonstrated a progressive increase of liver parenchyma and hypervascular liver lesion CNRs from high to lower energy levels in monoenergetic images, reaching the peak at 40 keV [11, 18, 19]. In particular, Marin et al. demonstrated that the maximal tumour-to-liver CNR for hypervascular lesion occurred at 40 keV in phantom and in vivo [11]. However, the study suggests, similar to our

results, that 55 keV may be a more conservative choice for liver imaging applications when noise is considered as an independent variable of image quality. These findings obtained with a second-generation scanner are in accordance with our observations; in addition, we further validated the value of low-keV data-sets for the detection of small hypervascular liver lesion using liver MRI as gold-standard. Similar to our study, Shuman et al. reported both best CNR and subjective scores at 50 keV [5], similar divergences among objective and subjective quality evaluation have already been described in previous papers in several anatomical districts [12, 20–25]. A possible explanation for these differences is that 50 keV demonstrated lower noise in comparison with 40 keV, resembling conventional images routinely used in clinical practice. Beyond the different study designs characterizing all the aforementioned studies, a common result is represented by the higher diagnostic performance of low keV virtual monoenergetic images compared to the traditional polyenergetic spectrum for the identification of solid parenchymal lesions, and the superior performances of VMI+ compared to VMI.CT accuracy in hypervascular lesions detection is significantly affected by lesion size. In a recent meta-analysis by Lee et al. [26], CT showed a summarized sensitivity for hypervascular liver lesion detection of 82 % for lesions ≥ 1 cm and only 31 % for lesions < 1 cm. In our study, 50 keV VMI+ provided the highest sensitivity for lesions

Fig. 4 Transverse sections from a dual-energy CT study of the liver in a 46-year-old man with hepatocellular carcinoma. Both readers correctly identified the ≥ 1 cm (*arrow-head*) and < 1 cm (*arrow*) diameter lesions at 50 keV VMI+ (**a**), and 70 keV VMI (**b**) dataset, while the smaller lesion was missed by both readers at M_0.6 (**c**). As an outside reference standard, contrast-enhanced MRI (**d**) confirmed the two hypervascular lesions. An intrahepatic portal vein branch is highlighted in all the datasets (*asterisk*)

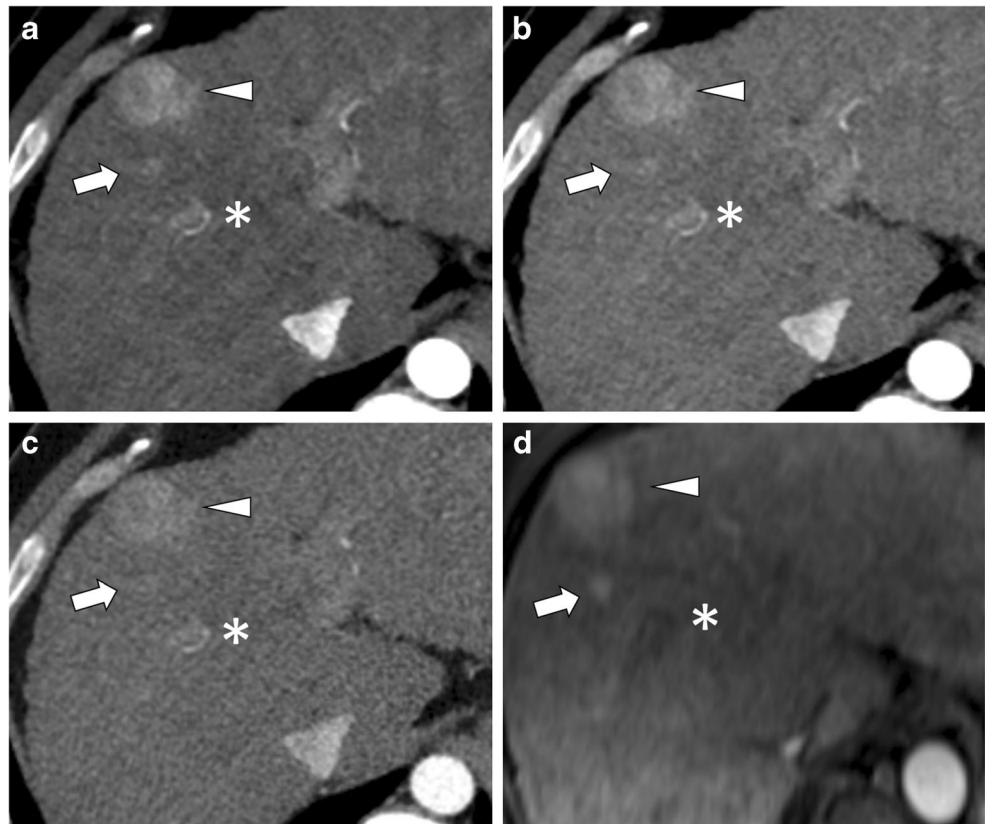
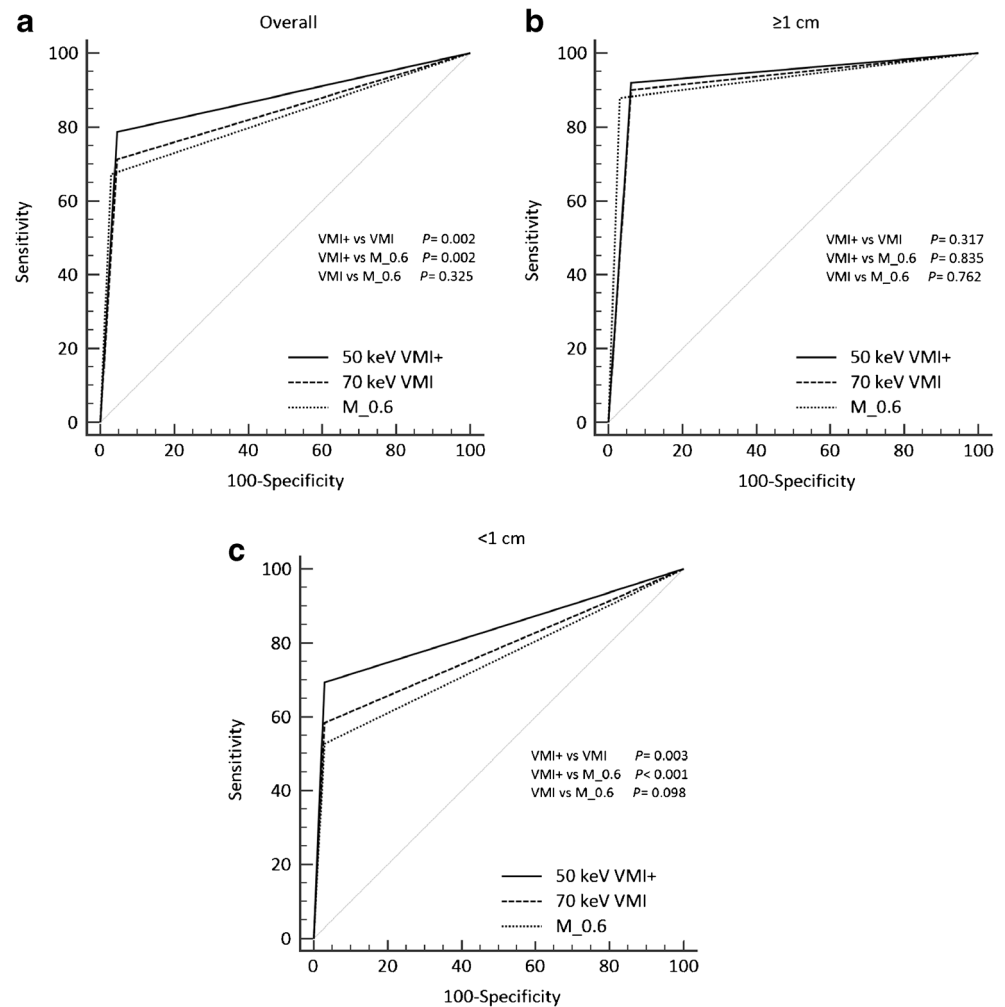


Fig. 5 Area under the receiver operating characteristic (ROC) curve (AUC) of the VMI+, VMI and M_0.6 datasets for all lesions (a), lesions ≥ 1 cm (b), and lesions < 1 cm (c). VMI+ always provided the largest AUC for lesion < 1 cm (all $p \leq 0.003$)



< 1 cm (69 %) among the three datasets, outperforming both VMI and M_0.6 datasets (58 % and 53 %, respectively) (Table 5). The improved diagnostic performance of VMI+ is presumably related to the higher VMI+ CNR, which allows for improved lesion conspicuity. Likewise, the lack of significant differences in the detection rates between VMI and M_0.6 datasets may be a consequence of the non-significant differences in liver lesion CNR between the two series. These results concur with previous published studies that analysed the standard VMI algorithm. Yu et al. [19] reported that 70 keV traditional monoenergetic images showed higher detectability of HCCs in comparison to conventional polyenergetic images. Similar results were reported by Lv et al. [27], who found that monoenergetic energy levels from 40 to 70 keV increased the detectability of small HCC lesions compared to conventional 140 kVp images, with the highest CNR found at 70 keV. Certain limitations of our study should be considered. First, the patient population of our prospective study was relatively small but with a large prevalence of hypervascular liver lesions; thus, larger studies are necessary to confirm our results. Second, no

histological information was used to classify the lesion detected. This study, however, was exclusively designed to evaluate the effect of monoenergetic images on the detection of hypervascular liver lesions, irrespective of histopathology. Third, our results are currently only valid for DECT and post-processing techniques using dual-source CT technology, and cannot be automatically translated to DECT solutions by other vendors. Finally, we acknowledge that other keV datasets demonstrating no significant difference in CNRs of hypervascular lesions could have provided similar diagnostic accuracy to the selected ones, since the difference in subjective image quality was small.

In conclusion, our results indicate that a 50-keV VMI+ dataset provides superior image quality and diagnostic accuracy for the detection of hypervascular liver lesions with a diameter < 1 cm, compared to VMI or M_0.6 reconstructions.

Funding This study has received funding by Siemens Healthineers (Malvern, PA, USA) through a research grant. The authors had control of the data and information submitted for publication.

Compliance with ethical standards

Guarantor The scientific guarantor of this publication is Dr. Carlo N. De Cecco.

Conflict of interest The authors of this manuscript declare relationships with the following companies:

Drs. De Cecco and Varga-Szemes receive institutional research support from Siemens.

Dr. Schoepf receives institutional research support from Astellas, Bayer, GE, Medrad, and Siemens.

Drs. Schoepf, De Cecco, and Varga-Szemes are consultants for Guerbet.

The other authors of this manuscript declare no relationships with any companies whose products or services may be related to the subject matter of the article.

Statistics and biometry Dr. Domenico De Santis kindly provided statistical advice for this manuscript.

Ethical approval Institutional Review Board approval was obtained.

Informed consent Written informed consent was obtained from all subjects (patients) in this study.

Methodology

- prospective
- diagnostic or prognostic study
- performed at one institution

References

1. Meier A, Wurnig M, Desbiolles L, Leschka S, Frauenfelder T, Alkadhi H (2015) Advanced virtual monoenergetic images: improving the contrast of dual-energy CT pulmonary angiography. *Clin Radiol* 70:1244–1251
2. Krauss B, Grant KL, Schmidt BT, Flohr TG (2015) The importance of spectral separation: an assessment of dual-energy spectral separation for quantitative ability and dose efficiency. *Invest Radiol* 50:114–118
3. Meyer M, Haubenreisser H, Schoepf UJ et al (2014) Closing in on the K edge: coronary CT angiography at 100, 80, and 70 kV-initial comparison of a second- versus a third-generation dual-source CT system. *Radiology* 273:373–382
4. Husarik DB, Gordic S, Desbiolles L et al (2015) Advanced virtual monoenergetic computed tomography of hyperattenuating and hypoattenuating liver lesions: ex-vivo and patient experience in various body sizes. *Invest Radiol* 50:695–702
5. Shuman WP, Green DE, Busey JM et al (2014) Dual-energy liver CT: effect of monochromatic imaging on lesion detection, conspicuity, and contrast-to-noise ratio of hypervascular lesions on late arterial phase. *AJR Am J Roentgenol* 203:601–606
6. Sudarski S, Apfaltrer P, Nance JW Jr et al (2014) Objective and subjective image quality of liver parenchyma and hepatic metastases with virtual monoenergetic dual-source dual-energy CT reconstructions: an analysis in patients with gastrointestinal stromal tumor. *Acad Radiol* 21:514–522
7. Yamada Y, Jinzaki M, Tanami Y, Abe T, Kuribayashi S (2012) Virtual monochromatic spectral imaging for the evaluation of hypovascular hepatic metastases: the optimal monochromatic level with fast kilovoltage switching dual-energy computed tomography. *Invest Radiol* 47:292–298
8. Delesalle MA, Pontana F, Duhamel A et al (2013) Spectral optimization of chest CT angiography with reduced iodine load: experience in 80 patients evaluated with dual-source, dual-energy CT. *Radiology* 267:256–266
9. Mileto A, Nelson RC, Samei E et al (2014) Dual-energy MDCT in hypervascular liver tumors: effect of body size on selection of the optimal monochromatic energy level. *AJR Am J Roentgenol* 203:1257–1264
10. Grant KL, Flohr TG, Krauss B, Sedlmair M, Thomas C, Schmidt B (2014) Assessment of an advanced image-based technique to calculate virtual monoenergetic computed tomographic images from a dual-energy examination to improve contrast-to-noise ratio in examinations using iodinated contrast media. *Invest Radiol* 49:586–592
11. Marin D, Ramirez-Giraldo JC, Gupta S et al (2016) Effect of a noise-optimized second-generation monoenergetic algorithm on image noise and conspicuity of hypervascular liver tumors: an in vitro and in vivo study. *AJR Am J Roentgenol*. <https://doi.org/10.2214/AJR.15.15512>:1-11
12. Albrecht MH, Trommer J, Wichmann JL et al (2016) Comprehensive comparison of virtual monoenergetic and linearly blended reconstruction techniques in third-generation dual-source dual-energy computed tomography angiography of the thorax and abdomen. *Invest Radiol* 51:582–590
13. Kondo H, Kanematsu M, Goshima S et al (2010) Body size indexes for optimizing iodine dose for aortic and hepatic enhancement at multidetector CT: comparison of total body weight, lean body weight, and blood volume. *Radiology* 254:163–169
14. Wichmann JL, Hardie AD, Schoepf UJ et al (2017) Single- and dual-energy CT of the abdomen: comparison of radiation dose and image quality of 2nd and 3rd generation dual-source CT. *Eur Radiol* 27:642–650
15. Marin D, Nelson RC, Samei E et al (2009) Hypervascular liver tumors: low tube voltage, high tube current multidetector CT during late hepatic arterial phase for detection—initial clinical experience. *Radiology* 251:771–779
16. Likert R (1932) A technique for the measurement of attitudes. *Arch Psychol* 140:155
17. DeLong ER, DeLong DM, Clarke-Pearson DL (1988) Comparing the areas under two or more correlated receiver operating characteristic curves: a nonparametric approach. *Biometrics* 44:837–845
18. Marin D, Caywood DT, Mileto A et al (2015) Dual-energy multidetector-row computed tomography of the hepatic arterial system: optimization of energy and material-specific reconstruction techniques. *J Comput Assist Tomogr* 39:721–729
19. Yu Y, Lin X, Chen K et al (2013) Hepatocellular carcinoma and focal nodular hyperplasia of the liver: differentiation with CT spectral imaging. *Eur Radiol* 23:1660–1668
20. Albrecht MH, Scholtz JE, Kraft J et al (2015) Assessment of an advanced monoenergetic reconstruction technique in dual-energy computed tomography of head and neck cancer. *Eur Radiol* 25:2493–2501
21. Frellesen C, Fessler F, Hardie AD et al (2015) Dual-energy CT of the pancreas: improved carcinoma-to-pancreas contrast with a noise-optimized monoenergetic reconstruction algorithm. *Eur J Radiol* 84:2052–2058
22. Hardie AD, Picard MM, Camp ER et al (2015) Application of an advanced image-based virtual monoenergetic reconstruction of dual source dual-energy CT data at low keV increases image quality for routine pancreas imaging. *J Comput Assist Tomogr* 39:716–720
23. Frellesen C, Kaup M, Wichmann JL et al (2016) Noise-optimized advanced image-based virtual monoenergetic imaging for improved visualization of lung cancer: comparison with traditional virtual monoenergetic imaging. *Eur J Radiol* 85:665–672
24. Martin SS, Pfeifer S, Wichmann JL et al (2017) Noise-optimized virtual monoenergetic dual-energy computed tomography:

- optimization of kiloelectron volt settings in patients with gastrointestinal stromal tumors. *Abdom Radiol (NY)* 42:718–726
25. Caruso D, De Cecco CN, Schoepf UJ et al (2017) Can dual-energy computed tomography improve visualization of hypoenhancing liver lesions in portal venous phase? Assessment of advanced image-based virtual monoenergetic images. *Clin Imaging* 41:118–124
 26. Lee YJ, Lee JM, Lee JS et al (2015) Hepatocellular carcinoma: diagnostic performance of multidetector CT and MR imaging—a systematic review and meta-analysis. *Radiology* 275:97–109
 27. Lv P, Lin XZ, Chen K, Gao J (2012) Spectral CT in patients with small HCC: investigation of image quality and diagnostic accuracy. *Eur Radiol* 22:2117–2124